Facile One-Pot Preparation of Chitosan/Calcium Pyrophosphate Hybrid Microflowers

Xiaoli Wang,[†,‡,§] Jiafu Shi,[†,§] Zheng Li,[†,§] Shaohua Zhang,[†,§] Hong Wu,[†,§] Zhongyi Jiang,*[,†,‡,§] Chen Yang,[†,§] and Chunyong Tian[†,§]

[†]Key Laboratory for Green Chemical Technology of Ministry of Education, School of Chemical Engineering and Technology, Tianjin University, Tianjin 300072, People's Republic of China

[‡]National Key Laboratory of Biochemical Engineering, Institute of Process Engineering, Chinese Academy of Sciences, Beijing 100190, People's Republic of China

[§]Collaborative Innovation Center of Chemical Science and Engineering (Tianjin), Tianjin 300072, People's Republic of China

Ⓢ Supporting Information

ABSTRACT: Flower-like chitosan/calcium pyrophosphate hybrid microparticles (microflowers) are prepared using a facile one-pot approach by combining ionotropic gelation with biomimetic mineralization. Chitosan—tripolyphosphate (CS-TPP) nanocomplexes are first synthesized through ionotropic gelation; meanwhile, excess TPP is partly hydrolyzed into pyrophosphate ions ($P_2O_7^{4-}$). Upon addition of $CaCl_2$, CS-TPP nanocomplexes serve as a versatile template, inducing in situ mineralization of $Ca_2P_2O_7$ and directing its growth and assembly into microflowers. The whole preparation process can be completed within half an hour. The as-prepared microflowers are composed of 23.0% CS-TPP nanocomplexes and 77.0% $Ca_2P_2O_7$ crystals. Mesopores (3.7 and 11.2 nm) and macropores coexist in the microflowers, indicating porous and hierarchical structures. The microflowers exhibit high efficiency in dye adsorption and enzymatic catalysis. Specifically, a high adsorption capacity of 520 mg g^{-1} for Congo red is achieved. And the immobilized enzyme retains about 85% catalytic activity compared with that of the free enzyme. The facile one-pot preparation process ensures the broad applications of the porous hybrid microflowers.

KEYWORDS: microflowers, chitosan, calcium pyrophosphate, mineralization, dye adsorption, enzyme immobilization
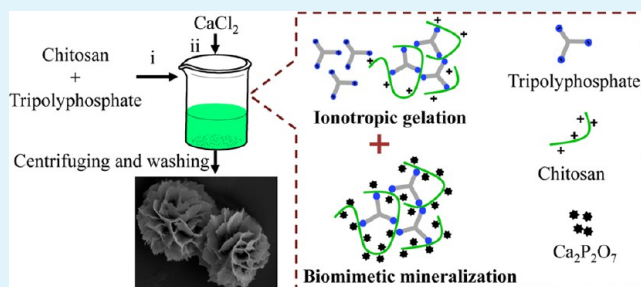
INTRODUCTION

Hierarchically structured porous materials, representing multiple level porosity integrated in a single scaffold, have recently triggered extensive research due to their potential technological impact in separation, catalysis and energy storage.[1−4] Natural bone is a hierarchically organized hybrid material and one of the toughest natural materials.[5] Calcium phosphate (CaP, such as $CaHPO_4$, $Ca_2P_2O_7$, $Ca_{10}(PO_4)_6(OH)_2$, etc.) is the main inorganic component of bone and responsible for its remarkable strength and stiffness,[6,7] which thus has excellent biocompatibility and affinity to biological substances, such as collagen, proteins, enzymes, cells and viruses.[8,9]

Numerous research efforts were devoted to the controllable preparation of calcium phosphate with diverse morphologies and hierarchical structure. Organic matrix mediated mineralization of CaP crystals was the predominant method, where organic molecules (collagen,[10,11] amino acids,[12,13] polyelectrolytes,[14] etc.) were used as the template and the sequestration agent. Other methods, including electrolytic deposition,[15] laser deposition,[16] hydrothermal synthesis,[17,18] and hydrolysis of salts,[19,20] were also reported. These studies demonstrate the successful preparation of hierarchical CaP, the preparation process often involves complicated operations or extreme operating conditions, such as high temperatures, organic solvents and microwaves. This often cause the irreversible denaturation of biomolecules. Liu et al. investigated the mild and facile formation of flower-like hydroxyapatite agglomerates at the interface of a bamboo/egg shell membrane after setting under ambient temperature for several days.[21,22] However, it was difficult to scale-up because of low reaction rate, arduous particle collection and the limited availability of materials. Recently, encouraging progress in the preparation of $CaHPO_4$/α-amylase hybrid nanoflowers with enhanced enzymatic activity was made by Zeng's group,[23] which was partly ascribed to flower-like hierarchical structures and biocompatibility of $CaHPO_4$. Continued research efforts toward seeking straightforward, inexpensive and rapid chemical methods to synthesize porous and hierarchical CaP, and understanding of their formation mechanism are highly required.

Chitosan (CS), a natural cationic polysaccharide, is widely used in combination with CaP to develop a hybrid scaffold for hard tissue engineering due to its nontoxicity, biofunctionality, biocompatibility and antibacterial nature.[20,24,25] CaP can be incorporated into chitosan by incubating chitosan in phosphate ions and calcium ions mixture (e.g., a simulated body fluid)[6,26,27] or by the straightforward mixing of chitosan with CaP.[25,28] Chitosan can be quickly cross-linked by tripolyphosphate (TPP) through ionotropic gelation to form nanocomplexes, which are biocompatible and can stabilize proteins against denaturation.[29−31] This method utilizes the reversible physical cross-linking, proceeded in aqueous environments and under mild conditions, and thus has attracted strong interest for drug delivery systems.[32] Furthermore, TPP is able to hydrolyze into pyro- and orthophosphate ions ($P_2O_7^{4-}$, PO_4^{3-}) in aqueous solution.[33,34] Hence, porous and hierarchical CaP may be prepared by using CS-TPP nanocomplexes as the template and TPP hydrolysates as the precursor.

In this study, a rapid one-pot approach to chitosan/calcium pyrophosphate hybrid microflowers is developed by combining ionotropic gelation with biomimetic mineralization. CS-TPP nanocomplexes were first synthesized through ionotropic gelation; meanwhile, part of TPP was hydrolyzed to $P_2O_7^{4-}$ anions, which were then adsorbed on the CS-TPP nanocomplexes. Upon addition of Ca^{2+}, the anisotropic growth of $Ca_2P_2O_7$ crystals on the CS-TPP nanocomplexes network resulted in the formation of hybrid microflowers. CS-TPP nanocomplexes provided a well-defined template and inducer for the nucleation and growth of $Ca_2P_2O_7$ crystals. The formation mechanism of the microflowers was tentatively elucidated. The as-prepared microflowers were characterized by scanning electron microscopy (SEM), X-ray diffraction (XRD), Fourier transform infrared spectroscopy (FTIR) and X-ray photoelectron spectroscopy (XPS) and Brunauer−Emmett−Teller (BET) surface area analyses. Moreover, the applicability of hybrid microflowers as a dye adsorption agent and enzyme immobilization carrier was explored.

■ MATERIALS AND METHODS

Materials. Chitosan (viscosity−average molecular weight: 450 kDa and 90.2% *N*-deacetylation degree) was purchased from Jinan Haidebei Marine Bioengineering Co. Ltd. (Jinan, China). Calcium chloride dehydrate ($CaCl_2 \cdot 2H_2O$, Bioxtra, ≥99.0% pure), sodium tripolyphosphate ($Na_5P_3O_{10}$, NaTPP), glacial acetic acid (CH_3COOH) and hydrogen peroxide (H_2O_2, 30 wt %) were purchased from Tianjin Guangfu Fine Chemical Research Institute (Tianjin, China). Catalase (CAT, hydrogen peroxide oxidoreductase; EC.1.11.1.6, C3145, 2000−5000 units/mg protein) from bovine liver, tris(hydroxymethyl)amiomethane (Tris) and fluorescein isothiocyanate (FITC) were purchased from Sigma-Aldrich Chemical Co. (USA). The water was purified by the Millipore Milli-Q before using in our experiments. CAT was labeled by FITC as follows: CAT was mixed with FITC in buffer solution (PBS, 50 mM, pH 8.0, [dye]/[enzyme] = 5) and then incubated overnight followed by dialysis against buffer solution (PBS, 50 mM, pH 7.0) for 72 h and water for 24 h.

Preparation of the Hybrid Microflowers. Chitosan (CS) was dissolved in 1 wt % acetic acid solution (2 mg mL^{-1}). 1.2 mL of 125 mg mL^{-1} TPP solution was added into 3 mL of 2 mg mL^{-1} CS solution upon stirring for 10 min. Then, 4.2 mL of 100 mM $CaCl_2$ was added into the above mixture upon stirring for another 10 min at room temperature. The hybrid microflowers were then obtained following centrifugation and washing.

Immobilization Efficiency and Loading Capacity of Enzyme. The immobilization efficiency was defined as the ratio of CAT amount

coprecipitated in the microflowers to the initial amount of CAT. The loading capacity was defined as the ratio of CAT amount coprecipitated in the microflowers to the weight of microflowers. The CAT concentrations with a known volume of washing solution was measured by the Bradford's method.[35] The immobilization efficiency and loading capacity were calculated according to eqs 1 and 2:

$$\text{immobilization efficiency (\%)} = \frac{(m - C_1V_1)}{m} \times 100\% \quad (1)$$

$$\text{loading capacity}(\text{mg g}^{-1}\text{ microflowers}) = \frac{(m - C_1V_1)}{W} \times 100\% \quad (2)$$

where m (mg) is the CAT amount introduced into the $CaCl_2$ solution; C_1 (mg mL^{-1}) and V_1 (mL) are the CAT concentration and volume of the supernate, respectively; W (g) is the weight of the microflowers.

Enzymatic Activity, Kinetic Constants (K_m and V_{max}) and Stabilities. The activity of CAT was assayed by the decrease of absorbance at 240 nm due to enzymatic H_2O_2 decomposition.[36] Specifically, the free or immobilized CAT was added to buffer solution (Tris−HCl, 50 mM, pH 7.0) with a H_2O_2 concentration of 19.58 mM. The decrease in absorbance was noted after reacting for 3 min at room temperature under stirring, and the enzymatic activity was determined according to eq 3:

$$2H_2O_2 \xrightarrow{\text{CAT}} 2H_2O + O_2 \quad (3)$$
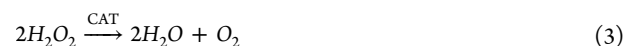
the relative activity was determined by comparing the activity of immobilized CAT with that of an equal amount of free CAT.

To determine K_m and V_{max} (K_m is the Michaelis−Menten contant; V_{max} is the maximum reaction rate), the activity was assayed at H_2O_2 concentrations varying from 20 to 70 mM. Enzymatic activity was determined in buffer solution (Tris−HCl, 50 mM, pH 7.0) under ambient temperature. V_{max} and K_m were calculated by the Michaelis−Menten model as shown in eq 4:

$$\frac{1}{V} = \frac{K_m}{V_{max}} \times \frac{1}{[S]} + \frac{1}{V_{max}} \quad (4)$$

where $[S]$ (mM) is the initial H_2O_2 concentration and V (mM min^{-1}) is the initial reaction rate.

The reusability of immobilized CAT was assessed by measuring the activity in each cycle. The CAT-containing microflowers were collected and washed with buffer solution (Tris−HCl, 50 mM, pH 7.0) after each batch and then added to the next cycle. The thermal stability was evaluated by measuring the residual activity after incubating at different temperature (30 to 70 °C) for 3 h.

Characterizations. SEM images of the microflowers were recorded with SEM (Nanosem 430). Elemental analysis of the microflowers was accomplished with an energy dispersive spectroscopy (EDS) instrument attached to a SEM instrument. Transmission electron microscopy (TEM) imaging of the microflowers was performed on a JEM-100CX II instrument. The ζ-potentials of microflowers surface were measured in water using a Brookhaven ζ-potential analyzer. Thermal gravimetric analysis (TGA) of the microflowers was conducted with a PerkinElmer Pyris analyzer by heating from 40 to 800 °C under air atmosphere. The microflowers were analyzed by a powder X-ray diffraction meter (XRD, D/MAX-2500). FTIR spectra of the microflowers were obtained using a Nicolet-6700 Fourier transform infrared spectrometer. The surface properties of the microflowers were characterized by X-ray photoelectron spectroscopy (XPS, Mg $K\alpha$) in a PerkinElmer PHI 1600 ESCA system. The pore-size distribution of the microflowers was determined by nitrogen adsorption−desorption isotherm measurements on a Tristar 3000 gas adsorption analyzer at 77 K. Pore-size-distribution curves were calculated based on the adsorption branch of nitrogen isotherms using the Barrett−Joyner−Halenda (BJH) method. UV−vis spectrophotometer (Hitachi U-3010) was used to measure the CAT concentration. Confocal laser scanning microscopy (CLSM)

Scheme 1. Preparation Process of the Hybrid Microflowers
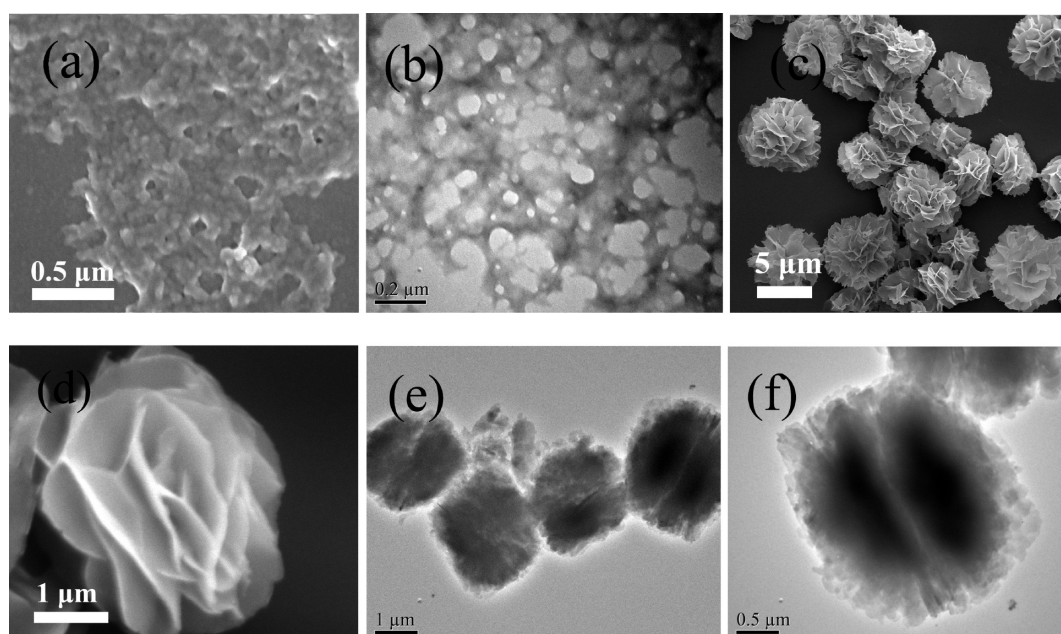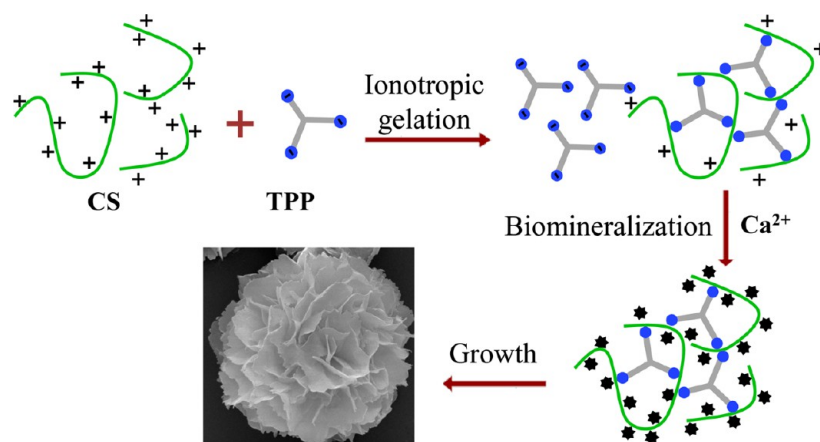
Figure 1. (a) SEM and (b) TEM images of the chitosan-TPP nanocomplexs, and SEM (c, d) and TEM (e, f) images of the hybrid microflowers.

images were obtained with a Leica TCS SP5 microscope, and the excitation wavelength for FITC-labeled CAT was set at 488 nm.

RESULTS AND DISCUSSION

Preparation and Characterizations of the Hybrid Microflowers. Scheme 1 illustrates the preparation process of the hybrid microflowers. Chitosan−tripolyphosphate (CS-TPP) nanocomplexes were synthesized by ionotropic gelation.[37] Upon the addition of TPP into the CS solution with stirring for 10 min, obvious turbidity changes of the solution were observed immediately. Simultaneously, the pH of the CS solution increased from 3.5 to 6.0, at which level the charge number of TPP was −3.3 and the ionization degree of CS was 0.8 according to the literature.[38] Hence, the spontaneous formation of CS-TPP nanocomplexes occurred due to intra- and intermolecular linkages between the positively charged CS and negatively charged TPP anions. SEM and TEM images (Figure 1a,b) indicated that the flocculent network structure of nanocomplexes. Subsequently, CaCl₂ was added into the CS/TPP mixture under stirring for another 10 min, and calcium phosphate would precipitate to generate spherical microflowers

through the regulation of CS. Microflowers were obtained after three centrifugation/water rinsing/redispersion cycles. The preparation process can be accomplished within 30 min. SEM images (Figure 1c,d) showed that the microflowers with a diameter of 3−5 μm were composed of well-defined 70 nm thick nanosheets. TEM images (Figure 1e,f) further verified the porous and hierarchical structures of the microflowers, which consisted of plate-shaped microparticles. Moreover, the center of microflowers was more porous according to the analysis of TEM. Quantitative analysis of the microflowers indicated that approximately 56 mg of the microflowers were collected from the solution. In addition, the one-pot preparation method was low cost and easily scale-up to obtain more than 10 g of the microflowers in one batch, and their morphology can be well maintained (Figure S1, Supporting Information).

Energy dispersive spectroscopy (EDS) analysis of the microflowers manifested the presence of C, O, P and Ca elements (Figure S2, Supporting Information). The presence of Al element was arisen from the aluminum foil for sample preparation. The atom ratio of P to Ca was 1.448 according to the analysis of EDS. Moreover, EDS mapping analysis
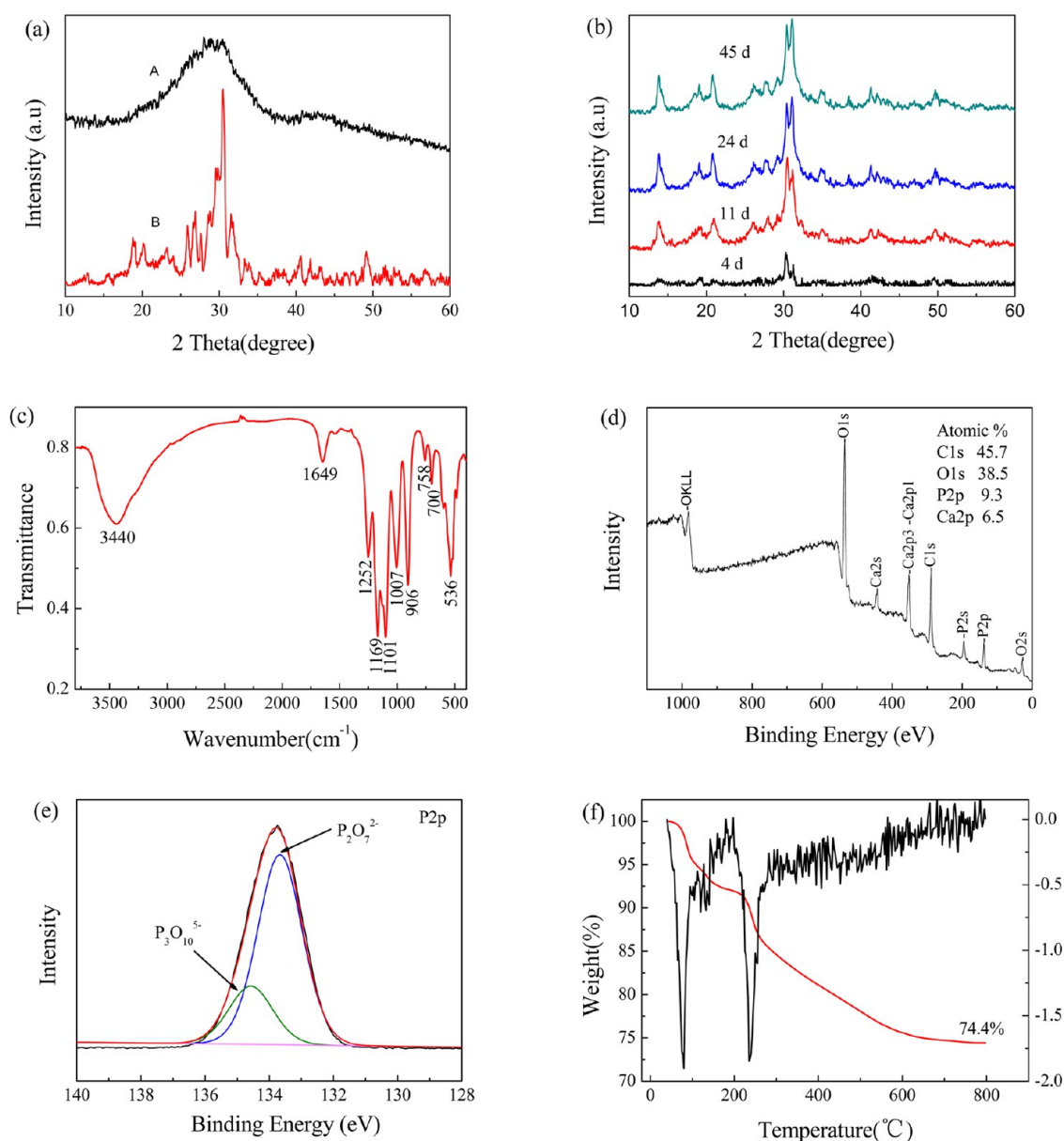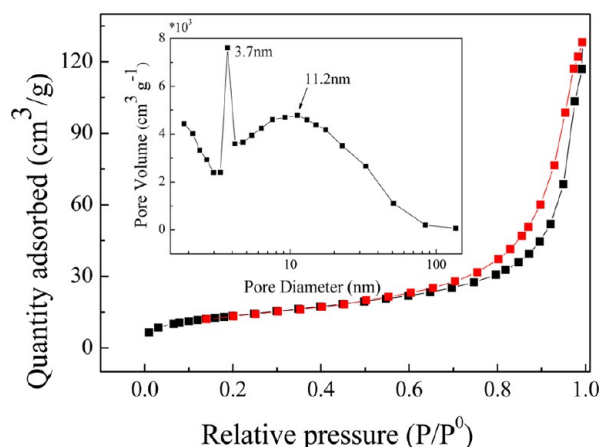
Figure 2. (a) XRD patterns of the microflowers before (A) and after thermal treatment (B), (b) XRD patterns of the microflowers after immersed in water for different times, and FTIR spectra (c), XPS spectra (d), the high-resolution P 2p spectrum (e), TGA and DTG curves (f) of the microflowers.

demonstrated that the Ca and P elements were predominantly distributed in the nanosheets of the microflowers (Figure.S3 Supporting Information).

XRD was employed to characterize the phase and crystal structure of the microflowers as shown in Figure 2a. XRD analysis proved the mineralized microflowers were calcium pyrophosphate hydrate (CPPD, $Ca_2P_2O_7 \cdot 2H_2O$, PDF#41-0490 and $Ca_2P_2O_7 \cdot 4H_2O$, PDF#44-0762) (Figure 2a-A). It should be noted that the broad peak was attributed to nanocrystalline nature of the microflowers. The presence of CPPD was ascribed to the hydrolysis of TPP to pyrophosphate ions.[33,39,40] To further verify the existence of CPPD, the microflowers were thermally treated at 400 °C for 4 h in air. The microflowers maintained their morphology well, as shown in the SEM images (Figure S4, Supporting Information) and were identified as calcium pyrophosphate (CPP, $Ca_2P_2O_7$, PDF#17-0499, #23-0871 and #09-0346) from the analysis of XRD (Figure 2a-B).

Thermal treatment accelerated the dehydration of CPPD. However, there did not exist calcium monophosphate in the microflowers, which suggested that TPP did not hydrolyze to orthophosphate ions (PO_4^{3-}) but to generate pyrophosphate ions ($P_2O_7^{4-}$) during the preparation process.[33] It has been demonstrated that TPP was first hydrolyzed to $P_2O_7^{4-}$, then $P_2O_7^{4-}$ was hydrolyzed to PO_4^{3-},[33,41] and the kinetics of the latter reaction was 1−2 orders of magnitude slower than that of the former.[34,41] Moreover, the solubility parameters of $Ca_2P_2O_7$ compounds were rather low,[42] leading to the rapid precipitation during the preparation. Therefore, calcium monophosphate did not exist in the fresh microflowers because the present preparation conditions (duration and temperature) did not allow further hydrolysis reaction of $P_2O_7^{4-}$. Furthermore, it has been demonstrated that $Ca_2P_2O_7$ is more biocompatible than hydroxyapatite, thus endowing the microflowers with favorable biocompatibility for diverse biorelated application fields.[43−45]

Figure 3. Nitrogen adsorption−desorption isotherms (inset was the pore size distribution curve by the BJH method) of the microflowers.

The corresponding standard XRD pattern can be found in the Figure S5c,d (Supporting Information).

To confirm if $P_2O_7^{4-}$ would hydrolyze during the storage, the microflowers were immersed in deionized water for different times and their XRD patterns were conducted (Figure 2b). The broad peak became sharp (30.4°) after immersing for 4 days, which clearly showed the presence of calcium pyrophosphate hydrate (CPPD, $Ca_2P_2O_7 \cdot 2H_2O$, PDF#41-0490 and $Ca_2P_2O_7 \cdot 4H_2O$, PDF#44-0762). When the immersion time was increased from 4 to 11 days, the main reflection peaks at 29.2° and 30.4°, which were consistent with the previous report,[46] intensified due to the increase of crystallized CPPD in the microflowers. Simultaneously, a new peak at 31.1° appeared, which can be assigned to the reflection of whitlockite phase ($Ca_3(PO_4)_2$, PDF#09-0169).[46,47] The formation of whitlockite suggested that part of pyrophosphate ions were hydrolyzed to orthophosphate ions after immersing the microflowers in water for 11 days. With the increase of immersion time to 25 days, the peak intensity at 31.1° increased, suggesting the further hydrolysis of pyrophosphate

ions. When the immersion time was extended to 45 days, the XRD pattern was similar to that of the microflowers immersed for 25 days, indicating that the hydrolysis equilibrium was reached. To conclude, calcium monophosphate did not exist in the fresh microflowers, while calcium pyrophosphate hydrate and whitlockite coexisted in the microflowers after immersion in water for more than 25 days.

FTIR spectra of the microflowers are shown in Figure 2c. The bands at 3440 and 1649 cm^{-1} were attributed to the stretching (νO−H) and bending (δHOH) vibrations of water molecules, respectively. The bands at 906, 758 and 700 cm^{-1} were characteristic of the ν_s POP symmetric vibrations, which was consistent with the infrared spectrum of $P_3O_{10}^{5-}$ and $P_2O_7^{4-}$.[27] The band at 758 cm^{-1} was characterized with the structure of a $P_3O_{10}^{5-}$ triphosphate.[48,49] The band at 536 cm^{-1} showed the bending vibration of phosphates with $P_3O_{10}^{5-}$ and $P_2O_7^{4-}$.[33,48,49] FTIR spectra further confirmed the existence of TPP and CPPD in the microflowers. Therefore, the microflowers were identified as the mixture of CS-TPP nanocomplexes and CPPD crystals. The absorption peaks of chitosan were not obvious because of their relatively low content in the microflowers.

XPS spectra of the microflowers (Figure 2d) also indicated the presence of C, O, P and Ca elements. The P/Ca ratio of microflowers calculated from the XPS spectrum was 1.437, which was very close to the result of the EDS analysis (1.448). And the theoretical atom ratio of P to Ca for CPPD was 1.0. Therefore, the microflowers contained 23.0% CS-TPP and 77.0% CPPD according to the ratio of P/Ca (the calculation process can be found in eq S1 (Supporting Information)). Moreover, the peak of P 2p at 133.6 and 134.5 eV corresponded to $P_2O_7^{4-}$ and $P_3O_{10}^{5-}$[40,50,51] with relative percentages of 76.8% and 23.2%, respectively, quantified by the normalized peak area in the high-resolution P 2p XPS spectrum (Figure 2e), which was very close to that obtained from the ratio of P/Ca.

The TGA curve of the microflowers (Figure 2f) presented two significant weight loss steps. The first weight loss step occurred at 40−200 °C (DTG peaks at 80.0 and 132.5 °C) and
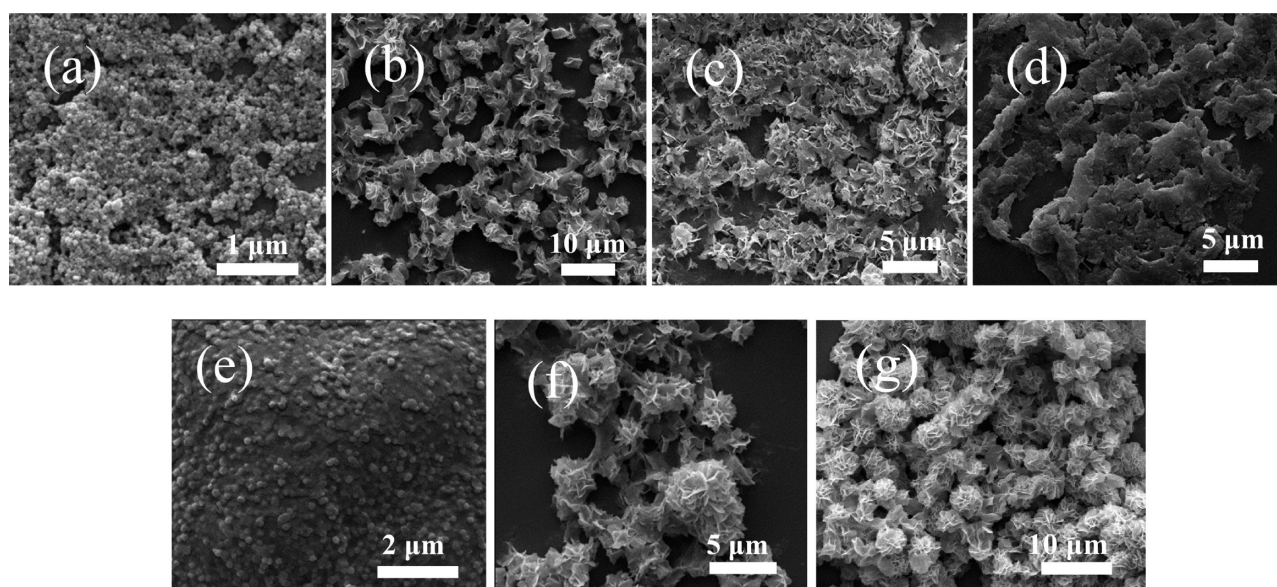
Figure 4. SEM images of microflowers prepared with varying concentration of CS (a) 0 mg mL^{-1}, (b) 1 mg mL^{-1}, (c) 5 mg mL^{-1} and (d) 10 mg mL^{-1}, and prepared with varying concentration of TPP (e) 5 mg mL^{-1}, (f) 30 mg mL^{-1} and (g) 125 mg mL^{-1}.
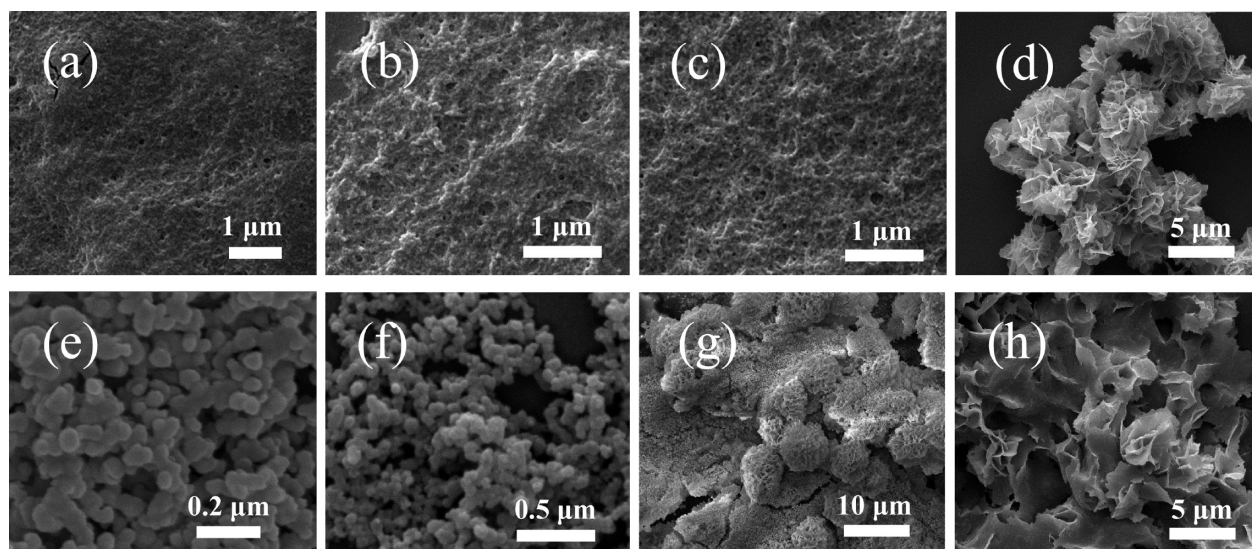
Figure 5. SEM images of microflowers prepared with varying concentration of CaCl$_2$ (a) 0 mM, (b) 25 mM, (c) 50 mM and (d) 200 mM, and varying mineralization time (e) 10 s, (f) 1 min, (g) 5 min and (h) 60 min.
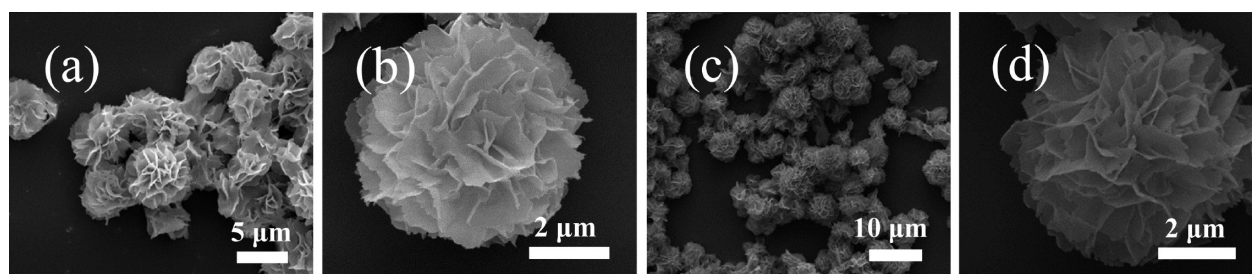
Figure 6. SEM images of the microflowers after stirred for 24 h at 600 rpm (a, b), and placing in water at 4 °C for 1 year (c, d).

had a mass loss of about 8.1% due to the loss of free, bound water. The second weight loss step occurred in the range 200–300 °C (DTG peaks at 235.0 °C) and was attributed to the decomposition of CS-TPP nanocomplexes in the microflowers. The weight loss between 200 and 800 °C was about 17.5%, which was ascribed to the content of CS-TPP nanocomplexes and crystal water in CPPD crystals. The mass fraction of inorganic component in the microflowers was 74.4% from the residual mass on heating to 800 °C.

N$_2$ adsorption–desorption was performed to analyze the porous structure of microflowers. As shown in Figure 3, at a lower relative pressure range ($P/P_0 > 0.6$), the hysteresis loop was clearly observed, which indicated the presence of mesopores in the microflowers. Moreover, adsorption did not reach saturation, and the capacity increased quickly at a higher relative pressure range ($P/P_0 > 0.9$), which meant the presence of larger interparticles mesopores and macropores. Therefore, the microflowers had a multiple level pore size distribution (a sharp band centered at pore size of 3.7 nm and a broad band between 4 and 100 nm), manifesting their porous and hierarchical structures. The mesopores were ascribed to the texture porosity formed by Ca$_2$P$_2$O$_7$ nanoparticles aggregation. And the macropores were arisen from the interspace among the nanosheets of microflowers. Moreover, the BET specific surface area of the microflowers was determined to be 51 m^2 g^{-1}, which was close to or even higher than those of calcium phosphate reported in the literature.[8,52–55] These porous and hierarchical structures may facilitate mass transport and consequently endow the microflowers with a broad range of applications. It

should be noted that the porosity of microflowers based on the BJH method was consistent with that observed by SEM and TEM.

The formation mechanism of microflowers was tentatively proposed. Ionotropic gelation happened after addition of TPP into the CS solution. At this stage, TPP cross-linked with CS to generate the precipitation of CS-TPP nanocomplexes through electrostatic interaction. Part of TPP was hydrolyzed to pyrophosphate ions (P$_2$O$_7^{4-}$). The hydrolysis reaction of TPP was accelerated by the CS solution containing acetic acids.[33] The hydrolyzed P$_2$O$_7^{4-}$ anions were adsorbed on the CS-TPP nanocomplexes due to their strong adsorption ability.[56] After the introduction of Ca^{2+}, the biomimetic mineralization of Ca$_2$P$_2$O$_7$ crystals occurred under the surface of the CS-TPP nanocomplexes network. Therefore, in these microenvironments, the CS-TPP nanocomplexes were used as the template to facilitate the rapid nucleation of Ca$_2$P$_2$O$_7$ crystals and guide their anisotropic growth on the CS-TPP nanocomplexes, leading to the formation of hybrid microflowers. To verify this mechanism, various factors affecting the microflowers formation were examined, including the concentrations of CS, TPP and CaCl$_2$, and the mineralization time. If no special instruction, the concentrations of CS, TPP and CaCl$_2$ were 2.0 mg mL^{-1}, 125 mg mL^{-1} and 100 mM, respectively, and the mineralization time was 10 min.

To understand the effect of CS content on the microflower structure, the experiments were conducted with the CS concentration varying from 0 to 10 mg mL^{-1}. Microflowers cannot be formed in the absence of CS; instead, nanoparticles
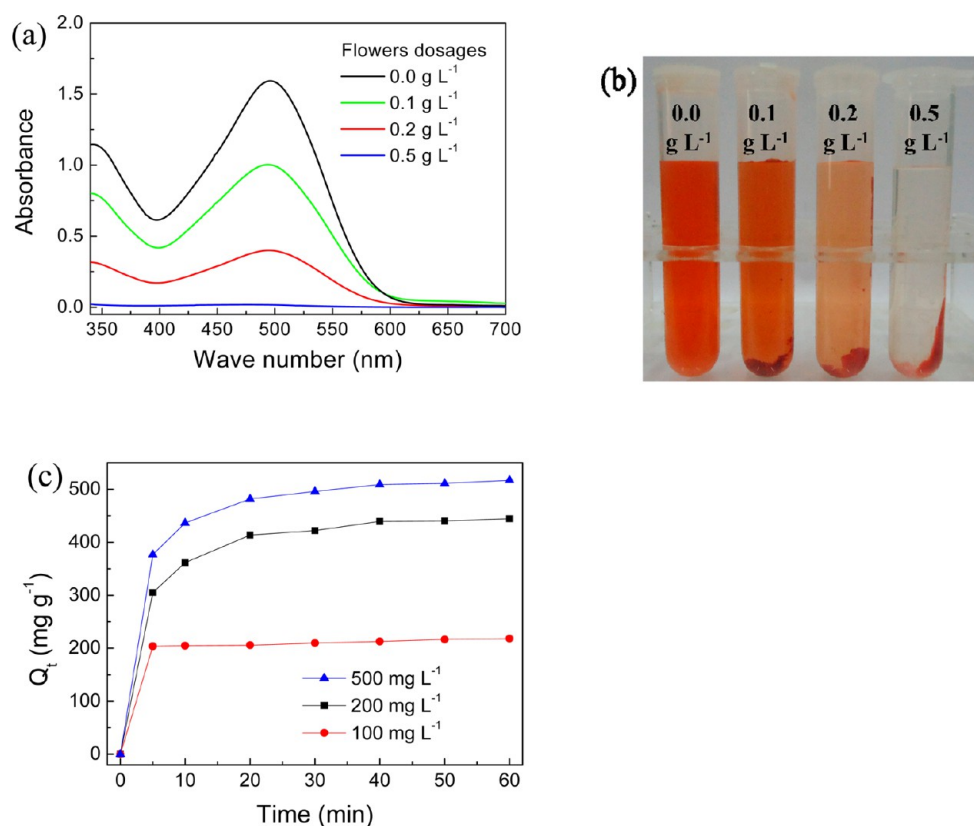
Figure 7. (a) UV−vis spectra of CR solution after being treated by the microflowers with different dosages; (b) photo of initial CR (100 mg L^{-1}) solution treated by the microflowers with different dosages; (c) time profiles of CR adsorption at different initial CR concentration with fixed microflowers dosage of 0.5 g L^{-1}.
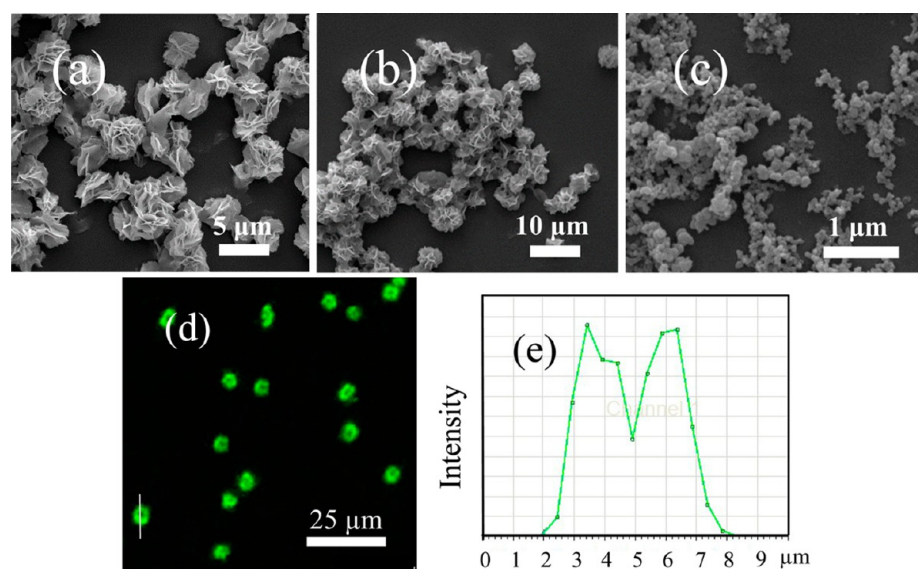
Figure 8. SEM images of microflowers coprecipitated with varying CAT amounts (a) 2.5 mg, (b) 5.0 mg and (c) 10.0 mg, and CLSM image (d) and fluorescence intensity (e) of the microflowers prepared with FITC-labeled CAT.

Table 1. Different Parameters of Microflowers Coprecipitated with Different Amounts of CAT

amount of CAT (mg)	immobilization efficiency (%)	loading capacity (mg g^{-1})	relative activity (%)
2.5	87.8	40	84.3
5.0	70.2	63	83.4
10.0	47.2	91	87.7

Table 2. Kinetic Parameters of Free and Immobilized CAT in the Microflowers

sample	K_m (mM)	V_{max} (mM min^{-1})
free CAT	59.5	27.6
immobilized CAT	62.5	22.2
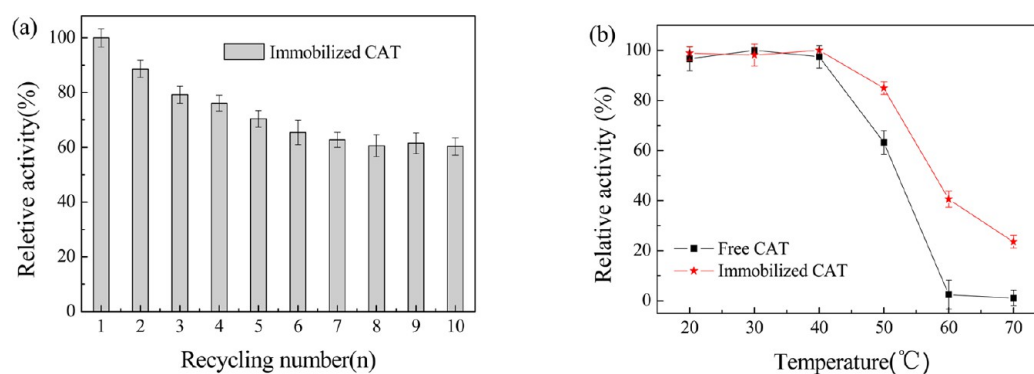
Figure 9. (a) Recycling stability of immobilized CAT in the microflowers; (b) thermal stability of free CAT and immobilized CAT in the microflowers.

about 45 nm in size were formed (Figure 4a). Microflowers began to appear when the concentration of CS was 1 mg mL^{-1} (Figure 4b) and 2 mg mL^{-1} (Figure 1c,d), suggesting that the formation of nanosheets required the presence of CS. Upon the increase in the concentration of CS to 5 mg mL^{-1}, nanosheets aggregates were observed instead of microflowers (Figure 4c). A further increase in the CS concentration resulted in thicker nanosheets aggregates (Figure 4d) because the abundant supply of CS-TPP nanocomplexes led to a very large number of nuclei for the growth of Ca$_2$P$_2$O$_7$ crystals. These results confirmed that the formation of microflowers was attributed to the anisotropic growth of Ca$_2$P$_2$O$_7$ crystals on the CS-TPP nanocomplexes. CS played a crucial role in regulating the biomimetic mineralization of Ca$_2$P$_2$O$_7$ crystals. In brief, microflowers cannot be obtained in the absence of CS, and thicker nanosheets aggregates would be observed when the CS concentration was too high.

Moreover, only a clear solution and virtually no precipitates were observed at low TPP concentrations. An increase in the concentration of TPP to 5 mg mL^{-1} resulted in nanoparticles with a size of 160 nm instead of microflowers (Figure 4e). It can be observed that, with increasing TPP concentrations to 30 mg mL^{-1}, microflowers started to appear (Figure 4f). Especially, a further increase in the TPP concentration to 125 mg mL^{-1} led to more integrated flower-like microparticles (Figure 4g). Therefore, an adequate amount of TPP was required in order to form enough CS-TPP nanocomplexes, which were then employed as the template for nucleation and the growth process. Furthermore, sufficient P$_2$O$_7^{4-}$ anions, a hydrolysis product of TPP, were also needed in order to ensure the growth of Ca$_2$P$_2$O$_7$ crystals.

Similarly, microflowers were formed only if the concentration of CaCl$_2$ was greater than 100 mM (Figure 5d). Otherwise, nanoparticles were generated at lower CaCl$_2$ concentration (Figure 5a–c). To further investigate the formation mechanism of microflowers, time-elapsing experiments were carried out, and the samples were taken at different time intervals between 10 s and 60 min. An appropriate mineralization time was required to guarantee the growth of microflowers. Nanoparticles with a diameter of around 50 nm would be generated instead of microflowers when the mineralization time was shorter than 5 min (Figure 5e,f). Upon an increase in the mineralization time to 5 min, a mixture of microflowers and nanoparticles was obtained (Figure 5g), suggesting the microflowers were growing from the nanoparticles. Well-defined microflowers were formed when the mineralization time increased to 10 min (Figure 1c,d). However, upon

continuous increases in the mineralization time to 60 min, thicker nanosheets aggregates would be observed (Figure 5h). By comparison, 10 min was the optimal mineralization time to form microflowers. These results further supported the above formation mechanism of hybrid microflowers. In this way, hybrid microflowers with Ca$_2$P$_2$O$_7$ as the inorganic component and chitosan as the organic component were developed with high yields.

The stability of the microflowers was evaluated by observing their morphology after stirring for 24 h at 600 rpm or placing in water at 4 °C. The microflowers well maintained their morphology without any breakage, suggesting their good mechanical stability after intense agitation (Figure 6a,b). Moreover, the microflowers were capable of being dispersed in aqueous media and remained stable for 1 year and more in water (Figure 6c,d). No pronounced changes in sizes and morphologies were found during the whole storage period, indicating that neither collapse nor aggregation occurred and the porous and hierarchical structures were well preserved. Good mechanical and storage stability of the hybrid microflowers were ascribed to the appropriate stability of calcium pyrophosphate.[45]

Potential Applications of the Hybrid Microflowers.
Dye Adsorption. The microflowers have porous and hierarchical structures and consequently may exhibit excellent adsorption properties. Herein, the as-synthesized microflowers were investigated for the removal of Congo red from water. Congo red (CR, Mw ≈ 696.7 Da, molecular charge: −2), an azoanionic dye, usually serves as a model pollutant to evaluate the removal capacity of adsorbents.[57,58] CR solutions were treated by the microflowers with different dosages and their UV−vis absorption spectra were conducted, as shown in Figure 7a, and the initial concentration of CR solutions was a fixed value (100 mg L^{-1}). The removal efficiency for CR increased with the increase of microflowers dosage. Particularly, CR can be nearly completely removed at a microflowers dosage of 0.50 g L^{-1}, which was also certified by the color change of CR solution from red to colorless (Figure 7b). Figure 7c showed the time profile of CR removal at different initial CR concentrations with a fixed microflowers dosage of 0.5 g L^{-1}. Under all CR concentrations, the adsorption achieved equilibrium quickly and mostly finished within 30 min, suggesting the fast adsorption rate of CR on the hybrid microflowers. As expected, the microflowers displayed a high adsorption capacity of 520 mg g^{-1} after adsorbing for 60 min at the initial CR concentration of 500 mg L^{-1}. So far, many materials were used to remove CR and their adsorption

capacities were generally below 500 mg g^{-1}.[2,58,59] Therefore, the microflowers with porous and hierarchical structures could become a promising adsorbent due to their high adsorption capacity and fast adsorption rate.

The ζ-potential of the hybrid microflowers was 39.7 mV at pH 7.0 and consequently the microflowers had positive surface charge and adsorbed CR by electrostatic attraction. To test this hypothesis, methylene blue (MB), with a smaller molecular weight (Mw $\approx$ 319.9 Da) but a positive charge, was chosen as adsorbate to assess the adsorption property of the microflowers.[60] And the microflowers exhibited an adsorption capacity of 1.2 mg g^{-1} after adsorbing for 60 min at the initial MB concentration of 20 mg L^{-1} with 0.5 g L^{-1} of the microflowers. This lower adsorption capacity should be ascribed to the electrostatic repulsion between MB and the microflowers, which further indicated that the adsorption of CR was driven by electrostatic attraction.

Enzyme Immobilization. The porous and hierarchical structures of hybrid microflowers endowed the substrate(s) and product(s) with efficient transport pathways and facilitatied the facile contact of the substrate(s) with enzyme molecules. The good biocompatibility of the microflowers ensured the well-retained bioactivity of enzyme molecules. Hence, the microflowers can be used as enzyme immobilization carriers/ supports. To this end, catalase (CAT) was immobilized into the microflowers via coprecipitation during microflowers preparation. A prescribed amount of CAT was dissolved into the CaCl$_2$ solution and then added into the mixture of chitosan and TPP to prepare the CAT-containing hybrid microflowers. SEM images (Figure 8a,b) showed that the morphology of microflowers was well maintained when the introduced amount of CAT was 2.5−5.0 mg. However, it should be noted that nanoparticles (∼100 nm) were formed instead of microflowers when the amount of CAT was 10.0 mg (Figure 8c). This was because CAT (pI 5.4) was negatively charged under neutral pH conditions and electrostatically interacted with the amine groups of CS, influencing ionotropic gelation of CS-TPP nanocomplexes. Therefore, the addition of CAT decreased the effective nucleation sites for calcium pyrophosphate formation and consequently the microflowers cannot be obtained. The result further confirmed the formation mechanism of the microflowers. Moreover, as shown in Table 1, with the increase of CAT, the immobilization efficiency was decreased although the CAT coprecipitated in microflowers was increased. Simultaneously, the CAT loading capacity was increased with the increase of CAT amount from 2.5 to 10.0 mg. Although the relative activities of immobilized CAT remained almost constant, around 85% of the enzymatic activity of the equivalent free CAT, indicating the microflowers (3−5 μm, micrometer scale) achieved comparative catalytic activity compared to nanoparticles (100 nm, nanometer scale). This phenomenon may be attributed to the abundant dispersive nanosheets of microflowers, leading to less mass transfer resistance. However, nanoparticles had a greater trend to self-assemble, which was detrimental to enzymatic activity although nanoparticles in diameter approximated the nanosheets of microflowers in thickness. Moreover, microflowers were more suitable for enzyme immobilization because they were easier to collect in comparison with nanoparticles (centrifuging at 764 g for 1 min vs 5437 g for 3 min). These favorable results were ascribed to hierarchical meso/macroporous structures of microflowers. In addition, the immobilized CAT in the microflowers exhibited slightly lower enzymatic activity

compared with that of free enzymes, whereas dramatically enhanced enzymatic activity was achieved with similar hybrid structures.[1,23] The reason for the enhanced activity was that metal ions in their carriers caused positive effects in activity upon interacting with the enzyme (Cu^{2+} for laccase and Ca^{2+} for α-amylase). However, in this study, the metal ions (Ca^{2+}) in the hybrid microflowers could not influence the activity of CAT. Besides, the slight decrease in activity was ascribed to the reduced enzyme flexibility after immobilized in the microflowers. The stability of CAT immobilized in the microflowers were investigated in the subsequent experiments, and the CAT-containing microflowers were prepared with 2.5 mg of CAT.

Confocal laser scanning microscopy (CLSM) was employed to confirm the location of CAT. CAT was first labeled by FITC and then coprecipitated in the microflowers. As expected, CAT was successfully entrapped within the microflowers according to CLSM imaging (Figure 8d). Similar to the result of TEM analysis, the fluorescence signal in the center of microflowers was relatively weak (Figure 8e), further confirmed the more porous structure, which may be caused by the steric hindrance when the microflowers grew.

To evaluate the enzymatic catalysis properties, the kinetic constants were calculated according to the Michaelis−Menten equation. The K_m for free CAT and immobilized CAT (Table 2) were comparable, suggesting that immobilization had little impact on the affinity of substrate toward CAT molecules. The slightly lowered V_{max} for the immobilized CAT suggested that immobilization restricted the enzyme's overall activity, possibly due to the reduced enzyme flexibility.

The potential of CAT immobilized in the microflowers for industrial applications was further analyzed by investigating the reusability, thermal stability and leakage. As shown in Figure 9a, after 10 cycles, about 60% activity was retained, and the decrease of activity was likely ascribed to the loss of microflowers during centrifugation operation between each cycle. Expectedly, the immobilized CAT displayed improved thermal stability, retaining 85.0% of its activity after incubating at 50 °C (only 63.7% for free CAT) (Figure 9b). Especially, free CAT was thoroughly inactive after incubating at 60 °C, whereas the immobilized CAT still had 40.5% of its activity. Enhanced thermal stability was probably due to interaction between CS and enzyme molecules. And the enzyme molecules confined in the nanoporous structures could create the synergistic effects that improved enzyme stability and rendered easier separation and reuse of enzymes.[61] Furthermore, no leakage of CAT was detected after stirring at 600 rpm for 48 h, because CAT was entrapped within the nanoparticles. Finally, it should be mentioned that the pH stability was not investigated since the microflowers were unstable under the acidic condition.

CONCLUSIONS

A facile one-pot method has been developed to prepare chitosan/calcium pyrophosphate hybrid microflowers by combining ionotropic gelation with biomimetic mineralization. The microflowers were obtained by mixing CS and TPP followed by the addition of CaCl$_2$. CS-TPP nanocomplexes network obtained by ionotropic gelation were acted as the template and inducer for the biomimetic mineralization of Ca$_2$P$_2$O$_7$ crystals. CS played a crucial role in regulating the nucleation and growth of Ca$_2$P$_2$O$_7$ crystals. The preparation process could be completed within half an hour. The as-prepared microflowers were composed of 23.0% CS-TPP

nanocomplexes and 77.0% $Ca_2P_2O_7$ crystals. The microflowers had hierarchical meso/macroporous structures, resulting in high dye adsorption properties for Congo red (520 mg g^{-1}) and enzyme immobilization efficiency. The hybrid microflowers were expected to be a promising candidate for application as adsorbents or catalyst carriers because of its porous and hierarchical structures as well as the facile and rapid preparation process.

■ ASSOCIATED CONTENT

Ⓢ Supporting Information

SEM images of the microflowers obtained by scaling-up preparation, EDS analysis of the microflowers, SEM image of the microflowers and corresponding EDS element mapping of Ca and P in the microflowers, SEM images of the microflowers after thermal treatment at 400 °C for 4 h in air, and XRD patterns of the microflowers before and after thermal treatment. This material is available free of charge via the Internet at http://pubs.acs.org.

■ AUTHOR INFORMATION

Corresponding Author

*Z. Jiang. E-mail: zhyjiang@tju.edu.cn. Fax: 86-22-27406646. Tel: 86-22-27406646.

Notes

The authors declare no competing financial interest.

■ ACKNOWLEDGMENTS

■ REFERENCES

(1) Ge, J.; Lei, J.; Zare, R. N. Protein−Inorganic Hybrid Nanoflowers. *Nat. Nanotechnol.* **2012**, 7, 428−432.

(2) Tian, P.; Han, X. Y.; Ning, G. L.; Fang, H. X.; Ye, J. W.; Gong, W. T.; Lin, Y. Synthesis of Porous Hierarchical MgO and Its Superb Adsorption Properties. *ACS Appl. Mater. Interfaces* **2013**, 5, 12411−12418.

(3) Zhang, X.; Görl, D.; Stepanenko, V.; Würthner, F. Hierarchical Growth of Fluorescent Dye Aggregates in Water by Fusion of Segmented Nanostructures. *Angew. Chem., Int. Ed.* **2014**, 53, 1270−1274.

(4) Li, J.; Zhang, H.; Zhang, Y.; Wang, M.; Zhang, F.; Nie, H. A Hierarchical Porous Electrode Using a Micron−Sized Honeycomb−like Carbon Material for High Capacity Lithium−Oxygen Batteries. *Nanoscale* **2013**, 5, 4647−4651.

(5) Duer, M.; Veis, A. Bone Mineralization: Water Brings Order. *Nat. Mater.* **2013**, 12, 1081−1082.

(6) Pu, X. M.; Sun, Z. Z.; Hou, Z. Q.; Yang, Y.; Yao, Q. Q.; Zhang, Q. Q. Fabrication of Chitosan/Hydroxylapatite Composite Rods with a Layer−by−Layer Structure for Fracture Fixation. *J. Biomed. Mater. Res., Part B* **2012**, 100, 1179−1189.

(7) Chen, F.; Bai, D.; Shao, C.; Wang, J.; Xi, P. Gelatin Functionalized Graphene Oxide for Mineralization of Hydroxyapatite: Biomimetic and *in Vitro* Evaluation. *Nanoscale* **2014**, 6, 5315−5322.

(8) Shum, H. C.; Bandyopadhyay, A.; Bose, S.; Weitz, D. A. Double Emulsion Droplets as Microreactors for Synthesis of Mesoporous Hydroxyapatite. *Chem. Mater.* **2009**, 21, 5548−5555.

(9) Dasgupta, S.; Bose, S. Reverse Micelle−Mediated Synthesis and Characterization of Tricalcium Phosphate Nanopowder for Bone Graft Applications. *J. Am. Ceram. Soc.* **2009**, 92, 2528−2536.

(10) Liu, Y.; Mai, S.; Li, N.; Yiu, C. K.; Mao, J.; Pashley, D. H.; Tay, F. R. Differences between Top−Down and Bottom−Up Approaches in Mineralizing Thick, Partially Demineralized Collagen Scaffolds. *Acta Biomater.* **2011**, 7, 1742−1751.

(11) Liu, Y.; Li, N.; Qi, Y.−p.; Dai, L.; Bryan, T. E.; Mao, J.; Pashley, D. H.; Tay, F. R. Intrafibrillar Collagen Mineralization Produced by Biomimetic Hierarchical Nanoapatite Assembly. *Adv. Mater.* **2011**, 23, 975−980.

(12) Cai, Y.; Yao, J. Effect of Proteins on the Synthesis and Assembly of Calcium Phosphate Nanomaterials. *Nanoscale* **2010**, 2, 1842−1848.

(13) Peytcheva, A.; Cölfen, H.; Schnablegger, H.; Antonietti, M. Calcium Phosphate Colloids with Hierarchical Structure Controlled by Polyaspartates. *Colloid Polym. Sci.* **2002**, 280, 218−227.

(14) Wang, Y.; Hassan, M. S.; Gunawan, P.; Lau, R.; Wang, X.; Xu, R. Polyelectrolyte Mediated Formation of Hydroxyapatite Microspheres of Controlled Size and Hierarchical Structure. *J. Colloid Interface Sci.* **2009**, 339, 69−77.

(15) Lin, D. Y.; Wang, X. X. Electrodeposition of Hydroxyapatite Coating on CoNiCrMo Substrate in Dilute Solution. *Surf. Coat. Technol.* **2010**, 204, 3205−3213.

(16) Zhang, M. Y.; Ye, C.; Erasquin, U. J.; Huynh, T.; Cai, C.; Cheng, G. J. Laser Engineered Multilayer Coating of Biphasic Calcium Phosphate/Titanium Nanocomposite on Metal Substrates. *ACS Appl. Mater. Interfaces* **2011**, 3, 339−350.

(17) Mi, P.; Kokuryo, D.; Cabral, H.; Kumagai, M.; Nomoto, T.; Aoki, I.; Terada, Y.; Kishimura, A.; Nishiyama, N.; Kataoka, K. Hydrothermally Synthesized PEGylated Calcium Phosphate Nanoparticles Incorporating Gd−DTPA for Contrast Enhanced MRI Diagnosis of Solid Tumors. *J. Controlled Release* **2014**, 174, 63−71.

(18) Delgado−López, J. M.; Frison, R.; Cervellino, A.; Gómez−Morales, J.; Guagliardi, A.; Masciocchi, N. Crystal Size, Morphology, and Growth Mechanism in Bio−Inspired Apatite Nanocrystals. *Adv. Funct. Mater.* **2013**, 24, 1090−1099.

(19) Furuichi, K.; Oaki, Y.; Imai, H. Preparation of Nanotextured and Nanofibrous Hydroxyapatite through Dicalcium Phosphate with Gelatin. *Chem. Mater.* **2006**, 18, 229−234.

(20) Gutiérrez, M. C.; Jobbagy, M.; Ferrer, M. L.; del Monte, F. Enzymatic Synthesis of Amorphous Calcium Phosphate−Chitosan Nanocomposites and Their Processing into Hierarchical Structures. *Chem. Mater.* **2008**, 20, 11−13.

(21) Zhang, Y.; Liu, Y.; Ji, X.-b. Fabrication of Flower-like Hydroxyapatite Agglomerates with the Assistant of Bamboo Membrane. *Mater. Lett.* **2011**, 65, 1982−1985.

(22) Zhang, Y.; Liu, Y.; Ji, X.; Banks, C. E.; Song, J. Flower-like Agglomerates of Hydroxyapatite Crystals Formed on an Egg-Shell Membrane. *Colloids Surf, B* **2011**, 82, 490−496.

(23) Wang, L. B.; Wang, Y. C.; He, R.; Zhuang, A.; Wang, X.; Zeng, J.; Hou, J. A New Nanobiocatalytic System Based on Allosteric Effect with Dramatically Enhanced Enzymatic Performance. *J. Am. Chem. Soc.* **2013**, 135, 1272−1275.

(24) Fosca, M.; Komlev, V. S.; Fedotov, A. Y.; Caminiti, R.; Rau, J. V. Structural Study of Octacalcium Phosphate Bone Cement Conversion in Vitro. *ACS Appl. Mater. Interfaces* **2012**, 4, 6202−6210.

(25) Bi, L.; Cheng, W.; Fan, H.; Pei, G. Reconstruction of Goat Tibial Defects Using an Injectable Tricalcium Phosphate/Chitosan in Combination with Autologous Platelet-rich Plasma. *Biomaterials* **2010**, 31, 3201−3211.

(26) Chiono, V.; Gentile, P.; Boccafoschi, F.; Carmagnola, I.; Ninov, M.; Georgieva, V.; Georgiev, G.; Ciardelli, G. Photoactive Chitosan Switching on Bone-like Apatite Deposition. *Biomacromolecules* **2010**, 11, 309−315.

(27) Yu, S.-H.; Wu, S.-J.; Wu, J.-Y.; Peng, C.-K.; Mi, F.-L. Tripolyphosphate Cross-Linked Macromolecular Composites for the Growth of Shape- and Size-Controlled Apatites. *Molecules* **2012**, 18, 27−40.

(28) Bao, C.; Chen, W.; Weir, M. D.; Thein−Han, W.; Xu, H. H. K. Effects of Electrospun Submicron Fibers in Calcium Phosphate Cement Scaffold on Mechanical Properties and Osteogenic Differ-

entiation of Umbilical Cord Stem Cells. *Acta Biomater.* **2011**, 7, 4037−4044.

(29) Goycoolea, F. M.; Lollo, G.; Remuñán−López, C.; Quaglia, F.; Alonso, M. J. Chitosan−Alginate Blended Nanoparticles as Carriers for the Transmucosal Delivery of Macromolecules. *Biomacromolecules* **2009**, 10, 1736−1743.

(30) Moura, M. J.; Faneca, H.; Lima, M. P.; Gil, M. H.; Figueiredo, M. M. *In Situ* Forming Chitosan Hydrogels Prepared via Ionic/ Covalent Co-Cross-Linking. *Biomacromolecules* **2011**, 12, 3275−3284.

(31) Zhang, J.; Tang, C.; Yin, C. Galactosylated Trimethyl Chitosan− Cysteine Nanoparticles Loaded with *Map4k4* siRNA for Targeting Activated Macrophages. *Biomaterials* **2013**, 34, 3667−3677.

(32) Huang, Y.; Lapitsky, Y. Salt-Assisted Mechanistic Analysis of Chitosan/Tripolyphosphate Micro- and Nanogel Formation. *Biomacromolecules* **2012**, 13, 3868−3876.

(33) Kandori, K.; Noguchi, Y.; Fukusumi, M.; Morisada, Y. Preparation of Spherical and Balloonlike Calcium Phosphate Particles from Forced Hydrolysis of $Ca(OH)_2$−Triphosphate Solution and Their Adsorption Selectivity of Water. *J. Phys. Chem. C* **2010**, 114, 6440−6445.

(34) Lampronti, G. I.; Artioli, G.; Oliva, L.; Ongaro, A.; Maretto, S.; Bonino, F.; Barbera, K.; Bordiga, S. Role of Phosphate Species and Speciation Kinetics in Detergency Solutions. *Ind. Eng. Chem. Res.* **2012**, 51, 4173−4180.

(35) Bradford, M. M. A Rapid and Sensitive Method for the Quantitation of Microgram Quantities of Protein Utilizing the Principle of Protein−Dye Binding. *Anal. Biochem.* **1976**, 72, 248−254.

(36) Çetinus, Ş. A.; Öztop, H. N. Immobilization of Catalase into Chemically Crosslinked Chitosan Beads. *Enzyme Microb. Technol.* **2003**, 32, 889−894.

(37) Gaspar, V.; Sousa, F.; Queiroz, J.; Correia, I. Formulation of Chitosan−TPP−pDNA Nanocapsules for Gene Therapy Applications. *Nanotechnology* **2011**, 22, 015101.

(38) Shu, X. Z.; Zhu, K. J. The Influence of Multivalent Phosphate Structure on the Properties of Ionically Cross−Linked Chitosan Films for Controlled Drug Release. *Eur. J. Pharm. Biopharm.* **2002**, 54, 235−243.

(39) Hossner, L.; Trostle, C.; Shahandeh, H. Hydrolysis of Cyclotri- and Cyclotetraphosphate in Soil. *Soil Sci. Soc. Am. J.* **2004**, 68, 74−81.

(40) Vasudevan, T.; Somasundaran, P.; Howie−Meyers, C.; Elliott, D.; Ananthapadmanabhan, K. Interaction of Pyrophosphate with Calcium Phosphates. *Langmuir* **1994**, 10, 320−325.

(41) Zhou, Y.; Carnali, J. O. Solid−State Hydrolysis of Calcium Tripolyphosphate Scales. *Langmuir* **2000**, 16, 5159−5168.

(42) Gras, P.; Teychene, S.; Rey, C.; Charvillat, C.; Biscans, B.; Sarda, S.; Combes, C. Crystallisation of a Highly Metastable Hydrated Calcium Pyrophosphate Phase. *CrystEngComm* **2013**, 15, 2294−2300.

(43) Lee, J. H.; Chang, B.-S.; Jeung, U.-O.; Park, K.-W.; Kim, M.-S.; Lee, C.-K. The First Clinical Trial of Beta−Calcium Pyrophosphate as a Novel Bone Graft Extender in Instrumented Posterolateral Lumbar Fusion. *Clin. Orthop. Surg.* **2011**, 3, 238−244.

(44) Vasant, S.; Joshi, M. Synthesis and Characterization of Pure and Zinc Doped Calcium Pyrophosphate Dihydrate Nanoparticles. *Eur. Phys. J.: Appl. Phys.* **2011**, 53, 10601−10606.

(45) Slater, C.; Laurencin, D.; Burnell, V.; Smith, M. E.; Grover, L. M.; Hriljac, J. A.; Wright, A. J. Enhanced Stability and Local Structure in Biologically Relevant Amorphous Materials Containing Pyrophosphate. *J. Mater. Chem.* **2011**, 21, 18783−18791.

(46) Leeuwenburgh, S.; Wolke, J.; Schoonman, J.; Jansen, J. Influence of Precursor Solution Parameters on Chemical Properties of Calcium Phosphate Coatings Prepared Using Electrostatic Spray Deposition (ESD). *Biomaterials* **2004**, 25, 641−649.

(47) Vallet-Regi, M.; Salinas, A.; Roman, J.; Gil, M. Effect of Magnesium Content on the *in Vitro* Bioactivity of $CaO−MgO−SiO_2−P_2O_5$ Sol−Gel Glasses. *J. Mater. Chem.* **1999**, 9, 515−518.

(48) Rosenthal, A. K.; Mattson, E.; Gohr, C. M.; Hirschmugl, C. J. Characterization of Articular Calcium-Containing Crystals by Synchrotron FTIR. *Osteoarthritis Cartilage* **2008**, 16, 1395−1402.

(49) Belaaouad, S.; Tridane, M.; Chennak, H.; Tamani, R.; Kenz, A.; Moutaabbid, M. Chemical Preparation, Thermal Behavior, Kinetic and Infrared Studies and Quantum Chemical Calculations of $Ca_3(P_3O_9)_2 \cdot 10H_2O$. *Phosphorus Res. Bull.* **2007**, 21, 60−70.

(50) Mangolini, F.; Rossi, A.; Spencer, N. D. Chemical Reactivity of Triphenyl Phosphorothionate (TPPT) with Iron: An ATR/FT-IR and XPS Investigation. *J. Phys. Chem. C* **2010**, 115, 1339−1354.

(51) Heuberger, R.; Rossi, A.; Spencer, N. D. Reactivity of Alkylated Phosphorothionates with Steel: A Tribological and Surface-Analytical Study. *Lubr. Sci.* **2008**, 20, 79−102.

(52) Dasgupta, S.; Bandyopadhyay, A.; Bose, S. Reverse Micelle-Mediated Synthesis of Calcium Phosphate Nanocarriers for Controlled Release of Bovine Serum Albumin. *Acta Biomater.* **2009**, 5, 3112−3121.

(53) Chaudhry, A. A.; Goodall, J.; Vickers, M.; Cockcroft, J. K.; Rehman, I.; Knowles, J. C.; Darr, J. A. Synthesis and Characterisation of Magnesium Substituted Calcium Phosphate Bioceramic Nanoparticles Made via Continuous Hydrothermal Flow Synthesis. *J. Mater. Chem.* **2008**, 18, 5900−5908.

(54) Sun, L.; Chow, L. C.; Frukhtbeyn, S. A.; Bonevich, J. E. Preparation and Properties of Nanoparticles of Calcium Phosphates with Various Ca/P Ratios. *J. Res. Natl. Inst. Stand. Technol.* **2010**, 115, 243−255.

(55) Deydier, E.; Guilet, R.; Sarda, S.; Sharrock, P. Physical and Chemical Characterisation of Crude Meat and Bone Meal Combustion Residue: "Waste or Raw Material?". *J. Hazard. Mater.* **2005**, 121, 141−148.

(56) Kandori, K.; Oda, S.; Tsuyama, S. Effects of Pyrophosphate Ions on Protein Adsorption onto Calcium Hydroxyapatite. *J. Phys. Chem. B* **2008**, 112, 2542−2547.

(57) Wang, B.; Wu, H.; Yu, L.; Xu, R.; Lim, T. T. Template-Free Formation of Uniform Urchin-like α-FeOOH Hollow Spheres with Superior Capability for Water Treatment. *Adv. Mater.* **2012**, 24, 1111−1116.

(58) Zhou, L.; He, B.; Huang, J. One-Step Synthesis of Robust Amine- and Vinyl-capped Magnetic Iron Oxide Nanoparticles for Polymer Grafting, Dye Adsorption, and Catalysis. *ACS Appl. Mater. Interfaces* **2013**, 5, 8678−8685.

(59) Wei, Z.; Xing, R.; Zhang, X.; Liu, S.; Yu, H.; Li, P. Facile Template-free Fabrication of Hollow Nestlike α-Fe_2O_3 Nanostructures for Water Treatment. *ACS Appl. Mater. Interfaces* **2012**, 5, 598−604.

(60) Zhang, Y.; Su, Y.; Chen, W.; Peng, J.; Dong, Y.; Jiang, Z. A Feasible Post-Treatment of Drying and Rewetting for Preparation of High-Flux Pluronic F127/Polyethersulfone Nanofiltration Membranes. *Ind. Eng. Chem. Res.* **2011**, 50, 4678−4685.

(61) He, W.; Min, D.; Zhang, X.; Zhang, Y.; Bi, Z.; Yue, Y. Hierachically Nanoporous Bioactive Glasses for High Efficiency Immobilization of Enzymes. *Adv. Funct. Mater.* **2013**, 24, 2206−2215.